

## Comparing nonperturbative models of the breakup of neutron-halo nuclei

P. Capel,<sup>1,2,3,\*</sup> H. Esbensen,<sup>4,†</sup> and F. M. Nunes<sup>5,‡</sup>

<sup>1</sup>*National Superconducting Cyclotron Laboratory, Michigan State University, East Lansing, Michigan 48824, USA*

<sup>2</sup>*Helmholtz-Insitut Mainz, Johannes Gutenberg-Universität, D-55128 Mainz, Germany*

<sup>3</sup>*Physique Quantique C.P. 165/82, Université Libre de Bruxelles (ULB), B-1050 Brussels, Belgium*

<sup>4</sup>*Physics Division, Argonne National Laboratory, Argonne, Illinois 60439, USA*

<sup>5</sup>*National Superconducting Cyclotron Laboratory and Department of Physics and Astronomy, Michigan State University, East Lansing, Michigan 48824, USA*

(Received 18 October 2011; revised manuscript received 20 February 2012; published 2 April 2012)

Breakup reactions of loosely bound nuclei are often used to extract structure and/or astrophysical information. Here we compare three nonperturbative reaction theories often used when analyzing breakup experiments, namely the continuum discretized coupled channel model, the time-dependent approach relying on a semiclassical approximation, and the dynamical eikonal approximation. Our test case consists of the breakup of  $^{15}\text{C}$  on Pb at 68 MeV/nucleon and 20 MeV/nucleon.

DOI: [10.1103/PhysRevC.85.044604](https://doi.org/10.1103/PhysRevC.85.044604)

PACS number(s): 24.10.-i, 25.60.Gc, 21.10.Gv, 27.20.+n

### I. INTRODUCTION

Due to the proximity to the particle threshold, loosely bound nuclei dissociate easily during collisions with nuclear targets. Consequently, they are often studied through breakup reactions, in which the loosely bound particle(s) dissociates from the core of the nucleus through interaction with the target. In the following, we focus on elastic breakup (i.e., a reaction in which the target is left in its ground state and all projectile fragments are detected in coincidence after dissociation). The use of breakup reactions for extracting properties of exotic nuclei is numerous and varied, including one-neutron halo systems [1–3], configuration-mixed systems [4,5], two-neutron halo systems [6–8], as well as proton rich systems [9–11]. While the shape of the energy distribution can tell us about the separation energy and the angular momentum of the ground state, the magnitude of the cross section is related to the asymptotic normalization of the ground state [12]. In addition, for two-particle halo systems, one also expects to obtain information on the correlations in the valence pair [13]. More recently, breakup reactions have proven to be a useful tool in exploring nuclei beyond the dripline and studying decay modes of resonant states [14–16].

If the reaction is dominated by the electromagnetic interaction, it is possible to connect the breakup cross section with the capture cross section [17,18]. This method, known as the Coulomb-dissociation method, is of interest to astrophysics because it can provide radiative-capture cross sections at very low relative energies where a direct measurement is not feasible. It also gives access to neutron-capture cross sections by unstable species, which are impossible to measure in the laboratory. It has been applied to a number of cases [3,9,18–20]. Providing confidence that the Coulomb-dissociation method works, neutron-capture cross sections for  $^{14}\text{C}(n,\gamma)^{15}\text{C}$  were extracted

from the Coulomb-dissociation data [3] using two independent methods [21,22] and perfect agreement was obtained when compared to direct measurements [23]. Similar efforts have been performed for the breakup of  $^8\text{B}$  [24–27].

The common feature of all the above-mentioned experiments is their need for a reliable reaction model in the analysis. One needs to be careful with separating nuclear and Coulomb processes, often nuclear-Coulomb interference is important and the dynamical effects in the continuum are crucial [18,24,28–31]. These results imply that, in general, perturbative approaches are not accurate enough for a reliable analysis of Coulomb-breakup measurements.

Hand in hand with the experimental advances, a number of nonperturbative breakup theories have been developed improving the method by which breakup reactions are studied (see Ref. [32] for a recent review). The many developments rely on different approximations, have separate advantages and shortcomings, and vary also in the level of complexity. We believe it is timely to compare these theories and understand the level of accuracy of the approximations made. In this work we compare the most common nonperturbative approaches to describe the breakup of a one-neutron halo nucleus that can be approximated by a two-body cluster. These are: (i) the continuum discretized coupled channel method (CDCC) [33,34], which is fully quantal and does not make approximations in the projectile-target dynamics, (ii) the time-dependent (TD) approach [35–38], which is based on a semiclassical approximation [39] that describes the projectile-target relative motion by a classical trajectory, and (iii) the dynamical eikonal approximation (DEA) [40,41], which relies on the eikonal approximation [42].

All three theories are built on the same three-body description of the reaction: the projectile  $P$ , described as a valence neutron  $f$  loosely bound to a core  $c$ , impinges on a target  $T$  considered as inert. The effective interaction between  $c$  and  $f$  is adjusted to reproduce known properties of the projectile, while the interactions between the projectile fragments and the target are simulated by optical potentials fitted to elastic-scattering data for the  $c$ - $T$  and  $f$ - $T$  systems.

\*pierre.capel@centraliens.net

†esbensen@phy.anl.gov

‡nunes@nscl.msu.edu

For the type of reactions we are interested in here, the CDCC method is the most accurate method available on the market but it is also the most computationally intensive and requires elaborate model-space studies. Developments that go beyond the inert-core and/or inert-target approaches, or extensions to  $N$ -body projectile clusters ( $N > 2$ ) are compromised by computational limitations. On the other hand, TD and DEA are not computationally intensive and are rather straightforward to set up. The question is whether these approximations can do a good job for the reactions of interest. To answer this question one needs to quantify the level of accuracy of the approximations introduced.

For a meaningful comparison, it is necessary that all three methods start from the exact same three-body Hamiltonian. Typical breakup observables are then compared to quantify the accuracy of the various approximations. The test case chosen is  $^{208}\text{Pb}(^{15}\text{C}, ^{14}\text{C}n)^{208}\text{Pb}$ , a case where we expect the three-body description to be adequate. Our study is performed at two energy regimes, one at a typical energy in fragmentation facilities (68 MeV/nucleon) [3] and the other at the higher-energy limit of isotope separation on-line (ISOL) facilities (20 MeV/nucleon). We ignore for practical reasons the effect of relativity.

In Sec. II we briefly summarize the three methods under scrutiny. The model inputs are given in Sec. III. In Sec. IV the results for breakup are presented, and we conclude in Sec. V. The details about the calculations in all three models can be found in the Addendum provided as supplemental material [43].

## II. BRIEF THEORETICAL DESCRIPTION

### A. Common framework

To study the breakup of a projectile  $P$  into a core  $c$  and a valence neutron  $f$  on a target  $T$ , we start from the (nonrelativistic) three-body Hamiltonian

$$H_{3b}(\mathbf{R}, \mathbf{r}) = \hat{T}_{\mathbf{R}} + H_0(\mathbf{r}) + U_{cT}(\mathbf{R}_c) + U_{fT}(\mathbf{R}_f), \quad (1)$$

expressed in the set of coordinates illustrated in Fig. 1. In Eq. (1),  $\hat{T}_{\mathbf{R}}$  is the kinetic-energy operator for the  $P$ - $T$  relative motion. The two-body Hamiltonian  $H_0$  describes the internal structure of the projectile

$$H_0(\mathbf{r}) = \hat{T}_{\mathbf{r}} + V_{cf}(\mathbf{r}), \quad (2)$$

where  $\hat{T}_{\mathbf{r}}$  is the  $c$ - $f$  kinetic-energy operator and  $V_{cf}$  is an effective potential, modeling the  $c$ - $f$  interaction. This potential is adjusted to reproduce the bound-state spectrum and low-energy scattering states of the projectile. The optical potential  $U_{cT}$  ( $U_{fT}$ ) describes the elastic scattering of the core (valence neutron) by the target and contains a Coulomb part and a nuclear part.

In all three methods, a partial wave expansion for the projectile states is used:

$$\phi_k^{lj1M}(\mathbf{r}) = \frac{u_k^{lj1M}(r)}{r} \{ [Y_l(\hat{\mathbf{r}}) \otimes \mathcal{X}_s]_j \otimes \mathcal{X}_{I_c} \}_{1M}, \quad (3)$$

where  $Y$  is a spherical harmonic [44] and  $\mathcal{X}$ s are spinors. The quantum number  $l$  is the orbital angular momentum of  $f$

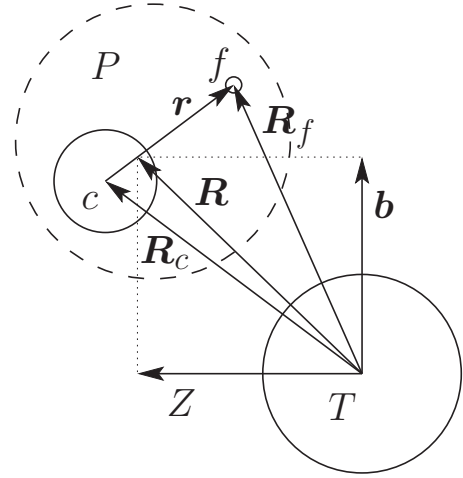


FIG. 1. Set of coordinates used in the reaction modeling. The longitudinal  $Z$  and transverse  $b$  components of  $\mathbf{R}$  are shown as well.

relative to  $c$ ,  $s(I_c)$  is the spin of the fragment  $f(c)$ , and the total angular momentum of the projectile is  $I$  with projection  $M$ . We denote by  $\phi_0$  the projectile bound state of (negative) energy  $E_0$ . For simplicity in this formulation we consider only one bound state. In this manner, all the other eigenstates of  $H_0$  correspond to positive energies  $E = \hbar^2/2\mu_{cf}k^2$ , with  $\mu_{cf}$  the  $c$ - $f$  reduced mass. They describe the  $c$ - $f$  continuum. Of course, the formulation can be easily extended to include bound excited states and we do include these in the application presented in Sec. IV.

Within this framework, the study of the  $P$ - $T$  collision reduces to solving the Schrödinger equation

$$H_{3b}\Psi(\mathbf{R}, \mathbf{r}) = E_{\text{tot}}\Psi(\mathbf{R}, \mathbf{r}) \quad (4)$$

with initial boundary condition:

$$\Psi(\mathbf{R}, \mathbf{r}) \xrightarrow{Z \rightarrow -\infty} e^{iK_0 Z} \phi_0(\mathbf{r}), \quad (5)$$

where the initial  $P$ - $T$  momentum  $\hbar\mathbf{K}_0$  is assumed along the  $Z$  axis. Its norm is related to the total energy  $E_{\text{tot}} = \hbar^2 K_0^2/2\mu_{PT} + E_0$ , with  $\mu_{PT}$  the  $P$ - $T$  reduced mass. There are different assumptions used in the treatment of the full three-body wave function  $\Psi$ . We capture the essential features in the following subsections.

### B. Continuum discretized coupled channel method

The full three-body wave function can always be expanded in terms of the complete set of projectile states  $\phi_k^{lj1M}$  as

$$\Psi(\mathbf{R}, \mathbf{r}) = \phi_0(\mathbf{r})\psi_0(\mathbf{R}) + \sum_{lj1M} \int dk \phi_k^{lj1M}(\mathbf{r})\psi_K^{lj1M}(\mathbf{R}), \quad (6)$$

such that the momentum  $\hbar k$  of the internal motion of  $c + f$  is related to the momentum  $\hbar K$  between the projectile center of mass and the target through energy conservation  $E_{\text{tot}} = \hbar^2 K^2/2\mu_{PT} + \hbar^2 k^2/2\mu_{cf}$ . An expansion involving an integral over momentum is not tractable, so in CDCC a discretization

of the projectile continuum is performed [33,45]. There are various ways of performing this discretization, and here we will use the so-called average method whereby  $\phi_k^{ljIM}$  is replaced by its average over a momentum bin  $[k_{p-1}, k_p]$ ,  $\tilde{\phi}_p^{ljIM}$  [45]. In this method the three-body wave function is approximated by

$$\Psi^{\text{CDCC}}(\mathbf{R}, \mathbf{r}) = \sum_{ljIM} \sum_{p=0}^N \tilde{\phi}_p^{ljIM}(\mathbf{r}) \psi_p^{ljIM}(\mathbf{R}), \quad (7)$$

with  $p = 0$  corresponding to the initial ground state and  $p \geq 1$  corresponding to the bin wave functions. The sum runs up to  $N$ , which is associated to the maximum projectile excitation energy  $E_{\text{max}}$  considered in the model space. In the end, the method needs to be independent of discretization and model space, and thus  $E_{\text{max}}$  needs to be large enough and the bin width needs to be small enough to accurately describe the process of interest [45].

When introducing expansion (7) into the full three-body equation (4), and after integrating over the angular variables and  $r$ , one arrives at the following coupled-channel equations in  $R$  [45]

$$\left[ -\frac{\hbar^2}{2\mu_{PT}} \left( \frac{d^2}{dR^2} - \frac{L(L+1)}{R^2} \right) + E_p - E_{\text{tot}} \right] \chi_{\alpha}^{J_{\text{tot}}}(R) + \sum_{\alpha'} i^{L'-L} V_{\alpha\alpha'}^{J_{\text{tot}}}(R) \chi_{\alpha'}^{J_{\text{tot}}}(R) = 0, \quad (8)$$

where  $L$  is the  $P$ - $T$  relative angular momentum,  $E_p$  is the midpoint energy of bin  $p$ , and  $\alpha$  is the index for the channel  $\{pljIL\}$ . The coupling potentials  $V_{\alpha\alpha'}^{J_{\text{tot}}}(R)$  are defined by,

$$V_{\alpha\alpha'}^{J_{\text{tot}}}(R) = \langle [\tilde{\phi}_p^{ljI} Y_L(\hat{\mathbf{R}})]_{J_{\text{tot}}} | U_{cT}(\mathbf{R}_c) + U_{fT}(\mathbf{R}_f) | [\tilde{\phi}_{p'}^{l'j'I'} Y_{L'}(\hat{\mathbf{R}})]_{J_{\text{tot}}} \rangle, \quad (9)$$

where  $J_{\text{tot}}$  is the total angular momentum resulting from the coupling of  $I$  and  $L$ . Equation (8) is solved with scattering boundary conditions at large distances,

$$\chi_{\alpha}^{J_{\text{tot}}}(R) \xrightarrow{R \rightarrow \infty} \frac{i}{2} \left[ H_{\alpha}^{-}(KR) \delta_{\alpha\alpha_i} - H_{\alpha}^{+}(KR) S_{\alpha\alpha_i}^{J_{\text{tot}}} \right], \quad (10)$$

where  $\alpha_i$  is the entrance channel, and  $H^{\pm}$  are Coulomb Hankel functions [45]. Breakup observables are then calculated from the resulting S matrix [34,46]. In the present work, we use the code FRESKO to numerically solve the set of coupled equations (8) [46,47]. The parameters of our calculations are given in the Addendum provided as a supplemental material of this article [43].

### C. Time-dependent model

It can be very demanding to solve the coupled-channel equations (8) numerically. To reduce the computational cost, other models have been developed. In the semiclassical approximation, the  $P$ - $T$  relative motion is approximated by a classical trajectory  $\mathbf{R}(t)$  [35–38]. Along that trajectory, the projectile experiences a time-dependent potential that simulates its interaction with the target. Assuming a quantal description

of the internal structure of the projectile, this approximation leads to the time-dependent Schrödinger equation,

$$i\hbar \frac{\partial}{\partial t} \Psi^{\text{TD}}(t, b, \mathbf{r}) = [H_0 + V_{PT}(t, \mathbf{r})] \Psi^{\text{TD}}(t, b, \mathbf{r}), \quad (11)$$

where  $b$  is the impact parameter characterizing the trajectory. The time-dependent potential  $V_{PT}$  appearing in this equation is the sum of the optical potentials of the three-body Hamiltonian (1), from which the potential that generates the trajectory is subtracted [36].

For Coulomb-dominated reactions, the potential that generates the classical trajectory is usually the bare  $P$ - $T$  Coulomb interaction, i.e.,

$$V_{PT}(t, \mathbf{r}) = U_{cT}[\mathbf{R}_c(t)] + U_{fT}[\mathbf{R}_f(t)] - \frac{Z_P Z_T e^2}{R(t)}, \quad (12)$$

where  $Z_P$  and  $Z_T$  are the atomic numbers of the projectile and the target, respectively.

The TD equation (11) has to be solved for all possible trajectories with the boundary condition that the projectile is initially in its ground state,

$$\Psi^{\text{TD}}(t \rightarrow -\infty, b, \mathbf{r}) = \phi_0(\mathbf{r}). \quad (13)$$

This is performed numerically by applying iteratively an approximation of the time-evolution operator to the initial wave function [35–38]. We use the algorithm detailed in Refs. [22,36]. At the end of the calculation, a breakup probability can be extracted for each trajectory by projecting the final wave function on the positive-energy eigenstates of  $H_0$ ,

$$\frac{dP_{\text{bu}}}{dk}(b) \propto \sum_{ljIM} |\langle \phi_k^{ljIM} | \Psi^{\text{TD}}(t \rightarrow +\infty, b) \rangle|^2. \quad (14)$$

Breakup observables can be calculated from these probabilities by proper integration over  $b$  [38]. Since these observables are obtained by summation over breakup probabilities and not over breakup amplitudes, the time-dependent technique cannot account for quantum interferences between different trajectories. We will see in Sec. IV the effects of such interferences.

### D. Dynamical eikonal approximation

More recently, the DEA has been developed from the comparison between the time-dependent model and the eikonal approximation [40,41]. It relies on the eikonal factorization of the three-body wave function (6) [42]

$$\Psi^{\text{DEA}}(\mathbf{R}, \mathbf{r}) = e^{iK_0 Z} \hat{\Psi}(\mathbf{R}, \mathbf{r}). \quad (15)$$

At sufficiently high energy, the deviation from the initial plane wave  $e^{iK_0 Z}$  of the  $P$ - $T$  relative motion is expected to be small. The dependence on  $\mathbf{R}$  of  $\hat{\Psi}$  is thus expected to be smooth. This enables us to neglect its second-order derivative in  $\mathbf{R}$  with respect to its first-order derivative

$$\Delta_{\mathbf{R}} \hat{\Psi}(\mathbf{R}, \mathbf{r}) \ll K_0 \partial / \partial Z \hat{\Psi}(\mathbf{R}, \mathbf{r}). \quad (16)$$

Therefore, introducing the factorization (15) into the three-body Schrödinger equation (4), leads to the DEA equation [41]

$$i \frac{\hbar^2 K_0}{\mu_{PT}} \frac{\partial}{\partial Z} \widehat{\Psi}(Z, \mathbf{b}, \mathbf{r}) = [(H_0 - E_0) + U_{cT}(\mathbf{R}_c) + U_{fT}(\mathbf{R}_f)] \widehat{\Psi}(Z, \mathbf{b}, \mathbf{r}), \quad (17)$$

where the dependence of the wave function on the longitudinal  $Z$  and transverse  $\mathbf{b}$  parts of the projectile-target coordinate  $\mathbf{R}$  has been made explicit (see Fig. 1).

The DEA equation (17) is mathematically equivalent to a time-dependent Schrödinger equation for a straight-line trajectory [see Eq. (11)]. It can therefore be solved using similar numerical techniques as in the time-dependent model [35–38]. As explained in Ref. [41], we use the algorithm detailed in Ref. [38]. The solution is obtained for each transverse component  $\mathbf{b}$  of the  $P$ - $T$  coordinate with the boundary condition

$$\widehat{\Psi}(Z \rightarrow -\infty, \mathbf{b}, \mathbf{r}) = \phi_0(\mathbf{r}). \quad (18)$$

Breakup amplitudes can then be extracted from the wave function

$$S_{\text{bu}}^{ljIM}(k, \mathbf{b}) \propto \langle \phi_k^{ljIM} | \widehat{\Psi}(Z \rightarrow +\infty, \mathbf{b}) \rangle. \quad (19)$$

Since no semiclassical approximation has been made to derive Eq. (17), the coordinates  $Z$  and  $\mathbf{b}$  are quantal variables. This enables us to take into account interferences between trajectories. This is noticeable by the fact that breakup observables are obtained in the DEA by integrating amplitudes (19) over  $\mathbf{b}$  and not breakup probabilities as in the time-dependent method of Sec. II C. The domain of validity of the approximation (16) remains to be tested by comparison to the other reaction models.

### III. MODEL INPUTS

In such a comparison, it is important to ensure that the inputs of all models are consistent. In this section, we summarize the various parameters that have been considered in the calculations presented in Sec. IV. More details can be found in the Addendum given as supplemental material [43].

All masses are calculated as mass number times the nucleon mass  $m_N = 931.5 \text{ MeV}/c^2$ . The effective potentials simulating the interactions between  $^{14}\text{C}$ ,  $n$ , and Pb are chosen identical in all three models. For the  $^{14}\text{C}$ - $n$  potential we take a Woods-Saxon central form factor (with depth  $V_{\text{ws}} = 63.023 \text{ MeV}$ , radius  $R_0 = 2.651 \text{ fm}$ , and diffuseness  $a = 0.6 \text{ fm}$ ) plus a spin-orbit term (with depth  $V_{\text{so}} = 23.761 \text{ MeVfm}^2$ , and the same radius and diffuseness as the central term). This potential reproduces the two bound states of  $^{15}\text{C}$ : the  $1/2^+$  ground state in the  $1s_{1/2}$  partial wave at the experimental energy  $E_{1s_{1/2}} = -1.218 \text{ MeV}$  and the excited  $5/2^+$  excited state as a  $0d_{5/2}$  state at  $E_{0d_{5/2}} = -0.478 \text{ MeV}$ .

The interactions between the Pb target and the projectile constituents are simulated by optical potentials chosen from the literature. The Becchetti and Greenlees parametrization [48] is used for the  $n$ -Pb potential. Since no  $^{14}\text{C}$ -Pb potential is available, we use, at 68 MeV/nucleon, a potential reproducing

the elastic scattering of  $^{16}\text{O}$  on Pb at 94 MeV/nucleon [49] and, at 20 MeV/nucleon, a potential fitted to the elastic scattering of  $^{16}\text{O}$  on Pb at 312.6 MeV (potential I3 of Ref. [50]). At both energies, the radius of the potential is scaled by  $(14^{1/3} + 208^{1/3})/(16^{1/3} + 208^{1/3})$  to correct for the difference between the sizes of  $^{14}\text{C}$  and  $^{16}\text{O}$ .

Convergence is an important part of the study and therefore was thoroughly tested for all cases. The parameter sets quoted in the Addendum provided as supplemental material [43] ensure an accuracy of at least 4% in the energy and angular distributions for all three models.

### IV. RESULTS

In this section we present the comparison for the breakup of  $^{15}\text{C}$  on  $^{208}\text{Pb}$  at two different beam energies: the first (68 MeV/nucleon) corresponds to an energy typical of fragmentation facilities for which data already exist [3], and the second (20 MeV/nucleon) serves as an example of the energies that will be available in facilities such as SPIRAL2 and FRIB. We present the breakup cross section as a function of either the  $^{14}\text{C}$ - $n$  relative energy  $E$  or the scattering angle  $\theta$  of the  $^{14}\text{C}$ - $n$  center of mass system.

The results for  $^{15}\text{C}$  on Pb at 68 MeV/nucleon are presented in Figs. 2 and 3. All three models predict nearly identical energy distributions (see Fig. 2): they differ by only 1–3% at the peak. They are also in excellent agreement with the RIKEN data [3], validating the reaction theory and the assumed single-particle nature of  $^{15}\text{C}$ . The aim of this analysis being to compare theories to each other, the theoretical cross sections have not been folded with the experimental energy resolution. Such a folding does not affect much the agreement between theory and experiment in the present case.

The angular distributions are shown in Fig. 3. The two quantal models, CDCC and DEA, agree very well with each other. In particular they exhibit similar diffraction patterns. The TD model does not exhibit any diffractive pattern. This diffraction pattern is a quantal effect corresponding to interferences between trajectories, an effect excluded in the semiclassical approximation. Nevertheless, the TD calculation

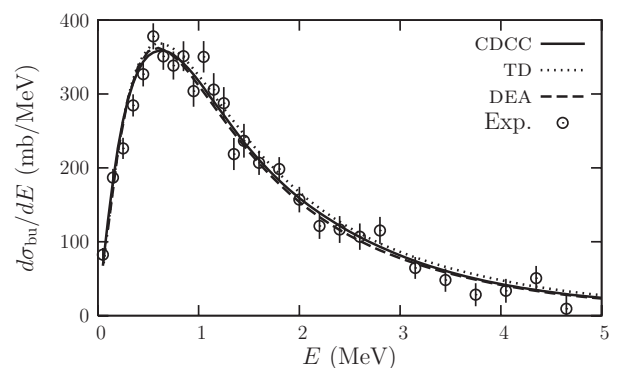


FIG. 2. Distribution for the breakup of  $^{15}\text{C}$  on Pb at 68 MeV/nucleon as a function of the  $^{14}\text{C}$ - $n$  relative energy. Comparison of three models: CDCC (solid), TD (dotted), and DEA (dashed). Experimental data from Ref. [3].

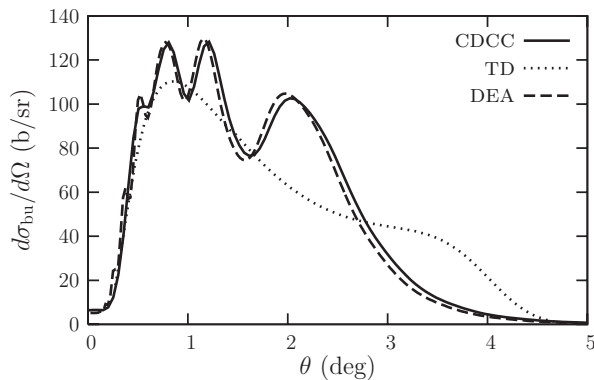


FIG. 3. Breakup cross section for  $^{15}\text{C}$  on Pb at 68 MeV/nucleon as a function of the scattering angle of the  $^{14}\text{C}$ - $n$  center of mass.

reproduces the general trend of the angular distribution at forward angles. This explains why, once integrated over the scattering angle, it produces a cross section nearly identical to the quantal models. Although DEA provides a good approximation to CDCC, a slight shift of about 3% in  $\theta$  is observed between both oscillatory patterns. However, at such beam energy, this small discrepancy is negligible compared to the uncertainties in the optical potentials.

Next we analyze the breakup of  $^{15}\text{C}$  on Pb at 20 MeV/nucleon. The energy distribution is displayed in Fig. 4 and the angular distribution in Fig. 5. If we first focus on the comparison of TD and CDCC models, excellent agreement in the energy distribution is found (a mere 1% difference at the peak). At this energy too, the semiclassical approximation fails at reproducing the correct diffraction pattern seen in the CDCC angular distribution, but, as seen at higher energy, the general trend of the cross section is well approximated by the TD model at forward angles. These results show that the TD model provides accurate breakup observables integrated over the scattering angle even at energies below the range of validity mentioned by Alder and Winther [39]. Because of its semiclassical approximation, the TD model cannot account for quantal interferences in the angular distributions. Nevertheless, it produces a qualitative estimate of the behavior of such distributions at forward angles.

The DEA energy distribution does not agree with the other two models at 20 MeV/nucleon; it is about 10% too high

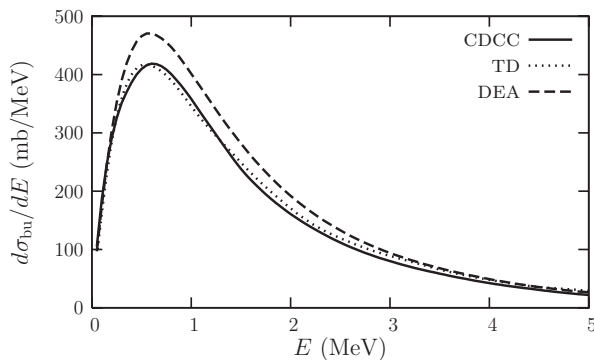


FIG. 4. Distribution for the breakup of  $^{15}\text{C}$  on Pb at 20 MeV/nucleon as a function of the  $^{14}\text{C}$ - $n$  relative energy.

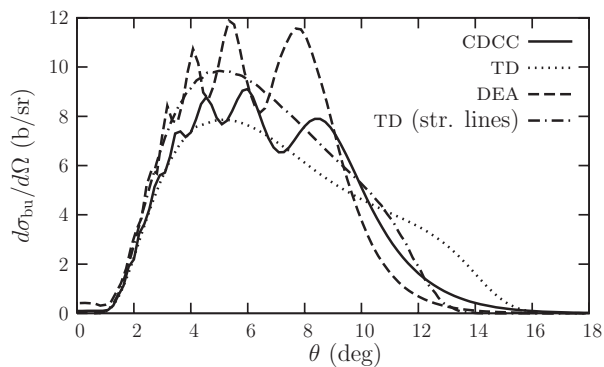


FIG. 5. Breakup cross section for  $^{15}\text{C}$  on Pb at 20 MeV/nucleon as a function of the scattering angle of the  $^{14}\text{C}$ - $n$  center of mass. In addition to CDCC, TD, and DEA results, a TD calculation using straight-line trajectories (dash-dotted) is shown.

at the peak. Due to its quantal nature, DEA does exhibit a diffraction pattern in the angular distribution, but the small discrepancy with CDCC found at 68 MeV/nucleon is now significantly increased as the DEA angular distribution peaks at more forward angles. The shift reaches here 10% in  $\theta$ . These results suggest that the difference observed between DEA and the other two models at low energy comes primarily from the lack of Coulomb deflection in DEA: Relying on the eikonal approximation, the DEA assumes that the incoming plane-wave motion of the projectile is not much perturbed by its interaction with the target (16). The DEA thus forces the projectile straight ahead into the high-field zone of the target, leading to a larger breakup cross section and a more forward angular distribution. On the contrary, the usual TD approach, being based on Coulomb trajectories, naturally includes the Coulomb deflection and hence reproduces CDCC calculations fairly well.

To test this hypothesis, we first repeat the time-dependent calculation using straight-line trajectories instead of hyperbolas (dash-dotted line in Fig. 5). Of course, this TD calculation does not exhibit any diffraction pattern. However, it provides a fair approximation of the general trend of the DEA angular distribution in the same way the usual TD calculation follows the CDCC one (compare the dotted and solid lines). This result was to be expected as the DEA equation (17) is mathematically equivalent to a time-dependent Schrödinger equation with straight-line trajectories (see Sec. IID). It nevertheless confirms the significance of Coulomb deflection in the reaction process. Second, we compare DEA to CDCC in a purely nuclear calculation (i.e., setting  $Z_T = 0$ ). The corresponding angular distributions are shown in Fig. 6. At large angles, both calculations are nearly identical. At forward angles, however, DEA underestimates CDCC and exhibits an oscillatory pattern shifted to larger angles. This difference with the Coulomb-dominated reaction is not very surprising as the nuclear interaction, being mostly attractive, tends to deflect the projectile within the high-field zone of the target. This very stringent test indicates that Coulomb deflection is not the only reason for the discrepancies observed in Figs. 4 and 5 and that other effects, such as nuclear deflection and/or couplings between various impact parameters  $b$ , are also significant.

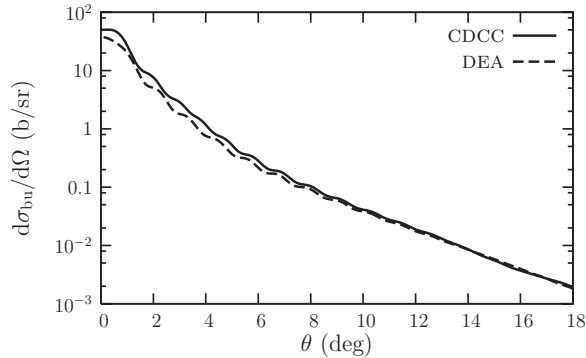


FIG. 6. Angular distributions for a hypothetical purely nuclear collision between  $^{15}\text{C}$  on Pb at 20 MeV/nucleon. DEA is compared to CDCC.

These results confirm that at low energies, the approximation (16) can no longer be performed as it suppresses part of the deflection of the projectile by the target, and/or some coupling effects between different  $bs$ . A correction of the DEA that could account for the Coulomb deflection would most likely provide a better description of Coulomb-dominated reactions at low energy.

To make sure that the qualitative features of our analysis do not depend on the particular choice of the core-target interaction, we have repeated the Coulomb-breakup calculations at 20 MeV/nucleon using the optical potentials used at 68 MeV/nucleon. As expected, the cross sections are sensitive to the parametrization of these potentials. The 68 MeV/nucleon potentials changes the energy distribution by 2–5% and reduces the amplitude of the oscillations of the diffraction pattern of the angular distribution. It also shifts that pattern by about 3% to larger angles. Nevertheless, the qualitative differences between the three models remain very similar.

The difference between CDCC and DEA seems to evolve smoothly when reducing the beam energy. At 40 MeV/nucleon, the energy distributions differ by a mere 5% at the maximum and the shift in the angular distributions is also about 5% in  $\theta$ .

## V. CONCLUSION

In this study, we perform a comparison of nonperturbative models of reactions involving loosely bound nuclei. We compare the continuum discretized coupled channel method (CDCC), the time-dependent (TD) approach, and the dynamical eikonal approximation (DEA) for the dissociation of a one-neutron halo nucleus on a heavy target. Starting from exactly the same three-body Hamiltonian, we calculate the energy distribution and angular distribution following the breakup of  $^{15}\text{C}$  on Pb at 68 MeV/nucleon and 20 MeV/nucleon in all three frameworks.

Our results show that for angle-integrated observables, TD works well and can be safely used in the analysis of data obtained at both intermediate-energy and low-energy facilities (i.e., on an energy range much larger than suggested in the original semiclassical approximation of Alder and Wither [39]). However, due to its classical treatment of trajectories,

TD cannot account for the diffraction pattern seen in the angular distributions. It provides only the general trend of these cross sections at forward angles.

The DEA approach is able to accurately reproduce the CDCC angular and energy distributions at 68 MeV/nucleon and therefore provides a computationally efficient alternative to CDCC without sacrificing accuracy. In contrast, at the lower beam energy, both energy and angular distributions in DEA cannot reproduce the CDCC results. DEA overestimates the energy distribution by 10% and, although the DEA angular distribution exhibits a diffraction pattern similar to that of CDCC, this pattern is shifted to more forward angles by about 10%. The primary cause of these discrepancies is the approximation (16) made in DEA. For Coulomb-dominated reactions, it amounts mostly to the absence of Coulomb deflection in that model. Thanks to the present analysis we now understand how to remedy the problem so that the domain of validity of DEA can be partially extended to the lower energies.

Although valid at all energies, CDCC is a reaction model that requires significant computational power. Our analysis shows that, depending on the beam energy and/or the observable considered, it can be reliably replaced by the TD model or the DEA. Since the DEA and TD techniques are computationally less expensive, these could allow for improving the description of the projectile in reaction models at a reasonable cost.

The present study corresponds to the first comparison of nonperturbative breakup models at intermediate energies. It quantitatively shows for which observables and energies the models agree and in which conditions their predictions should be considered with caution. This provides for the first time the range of validity of the three models. The projectile description being quite general, these results can be extended to other neutral loosely bound systems with confidence. Note that they cannot be readily extended to charged systems as the mechanism of the Coulomb dissociation of proton-halo nuclei differs from that of neutron halos: The former involves more significant  $E2$  transitions and stronger higher-order dynamical effects than the latter [24–26,30,31].

Being focused on the comparison between three reaction models, the present study has been performed within the framework of nonrelativistic quantum mechanics. However, relativistic effects may start to play a role at energies around 100 MeV/nucleon [51]. Our conclusions should therefore not readily be extended to such energies. A detailed analysis of the effect of relativity in breakup reactions is planned in the near future.

## ACKNOWLEDGMENTS

We thank I. J. Thompson for his help in running FRESKO and the support of the High-Performance Computer Center of Michigan State University (MSU) while performing our calculations. P.C. and F.M.N. were supported by the National Science Foundation, Grant No. PHY-1068571, and the Department of Energy under Contracts No. DE-FG52-08NA28552 and No. DE-SC0004087. H.E. was supported by the US Department of Energy, Office of Nuclear Physics, under Contract No. DE-AC02-06CH11357.

- [1] T. Nakamura *et al.*, *Phys. Rev. Lett.* **83**, 1112 (1999).
- [2] R. Palit *et al.*, *Phys. Rev. C* **68**, 034318 (2003).
- [3] T. Nakamura *et al.*, *Phys. Rev. C* **79**, 035805 (2009).
- [4] D. Cortina-Gil *et al.*, *Phys. Rev. Lett.* **93**, 062501 (2004).
- [5] T. Nakamura *et al.*, *Phys. Rev. Lett.* **103**, 262501 (2009).
- [6] T. Aumann *et al.*, *Phys. Rev. C* **59**, 1252 (1999).
- [7] T. Nakamura *et al.*, *Phys. Rev. Lett.* **96**, 252502 (2006).
- [8] K. Tanaka *et al.*, *Phys. Rev. Lett.* **104**, 062701 (2010).
- [9] F. Schümann *et al.*, *Phys. Rev. C* **73**, 015806 (2006).
- [10] J. F. Liang *et al.*, *Phys. Rev. C* **67**, 044603 (2003).
- [11] M. Mazzocco *et al.*, *Phys. Rev. C* **82**, 054604 (2010).
- [12] P. Capel and F. M. Nunes, *Phys. Rev. C* **73**, 014615 (2006); *ibid.* **75**, 054609 (2007).
- [13] K. Hagino, H. Sagawa, T. Nakamura, and S. Shimoura, *Phys. Rev. C* **80**, 031301 (2009).
- [14] C. C. Hall *et al.*, *Phys. Rev. C* **81**, 021302 (2010).
- [15] M. Thoennessen, S. Yokoyama, and P. G. Hansen, *Phys. Rev. C* **63**, 014308 (2000).
- [16] C. R. Hoffman *et al.*, *Phys. Rev. C* **83**, 031303 (2011).
- [17] G. Baur, C. A. Bertulani, and H. Rebel, *Nucl. Phys. A* **458**, 188 (1986).
- [18] G. Baur, K. Hencken, and D. Trautmann, *Prog. Part. Nucl. Phys.* **51**, 487 (2003).
- [19] N. C. Summers and F. M. Nunes, *Phys. Rev. C* **70**, 011602 (2004).
- [20] F. Hammache *et al.*, *Phys. Rev. C* **82**, 065803 (2010).
- [21] N. C. Summers and F. M. Nunes, *Phys. Rev. C* **78**, 011601 (2008).
- [22] H. Esbensen, *Phys. Rev. C* **80**, 024608 (2009).
- [23] R. Reifarh *et al.*, *Phys. Rev. C* **77**, 015804 (2008).
- [24] H. Esbensen, G. F. Bertsch, and K. A. Snover, *Phys. Rev. Lett.* **94**, 042502 (2005).
- [25] K. Ogata, S. Hashimoto, Y. Iseri, M. Kamimura, and M. Yahiro, *Phys. Rev. C* **73**, 024605 (2006).
- [26] G. Goldstein, P. Capel, and D. Baye, *Phys. Rev. C* **76**, 024608 (2007).
- [27] E. G. Adelberger *et al.*, *Rev. Mod. Phys.* **83**, 195 (2011).
- [28] F. M. Nunes and I. J. Thompson, *Phys. Rev. C* **59**, 2652 (1999).
- [29] M. S. Hussein, R. Lichtenthäler, F. M. Nunes, and I. J. Thompson, *Phys. Lett. B* **640**, 91 (2006).
- [30] H. Esbensen and G. F. Bertsch, *Phys. Rev. C* **66**, 044609 (2002).
- [31] P. Capel and D. Baye, *Phys. Rev. C* **71**, 044609 (2005).
- [32] D. Baye and P. Capel, *Breakup Reaction Models for Two- and Three-Cluster Projectiles in Cluster in Nuclei, Vol. 2*, Lecture Notes in Physics **848**, edited by C. Beck (Springer, Berlin, 2012), p. 121, see also [arXiv:1011.6427](https://arxiv.org/abs/1011.6427) (2010).
- [33] N. Austern, Y. Iseri, M. Kamimura, G. Rawitscher, and M. Yahiro, *Phys. Rep.* **154**, 125 (1987); M. Yahiro, N. Nakano, Y. Iseri, and M. Kamimura, *Prog. Theo. Phys.* **67**, 1464 (1982); *Prog. Theo. Phys. Suppl.* **89**, 32 (1986).
- [34] J. A. Tostevin, F. M. Nunes, and I. J. Thompson, *Phys. Rev. C* **63**, 024617 (2001).
- [35] T. Kido, K. Yabana, and Y. Suzuki, *Phys. Rev. C* **50**, R1276 (1994).
- [36] H. Esbensen, G. F. Bertsch, and C. A. Bertulani, *Nucl. Phys. A* **581**, 107 (1995).
- [37] S. Typel and H. H. Wolter, *Z. Naturforsch. A* **54**, 63 (1999).
- [38] P. Capel, D. Baye, and V. S. Melezhik, *Phys. Rev. C* **68**, 014612 (2003).
- [39] K. Alder and A. Winther, *Electromagnetic Excitation* (North-Holland, Amsterdam, 1975).
- [40] D. Baye, P. Capel, and G. Goldstein, *Phys. Rev. Lett.* **95**, 082502 (2005).
- [41] G. Goldstein, D. Baye, and P. Capel, *Phys. Rev. C* **73**, 024602 (2006).
- [42] R. J. Glauber, in *High Energy Collision Theory*, Lectures in Theoretical Physics, Vol. 1, edited by W. E. Brittin and L. G. Dunham (Interscience, New York, 1959), p. 315.
- [43] See Supplemental Material at <http://link.aps.org/supplemental/10.1103/PhysRevC.85.044604> for details about the calculations in all three models.
- [44] M. Abramowitz and I. A. Stegun, *Handbook of Mathematical Functions* (Dover, New York, 1970).
- [45] I. Thompson and F. Nunes, *Nuclear Reactions for Astrophysics* (Cambridge University Press, Cambridge, 2009).
- [46] I. J. Thompson, *Comput. Phys. Rep.* **7**, 167 (1988).
- [47] I. J. Thompson, *Fresco: Coupled reaction channels calculations* (2011) [<http://www.fresco.org.uk/>].
- [48] F. D. Becchetti Jr. and G. W. Greenlees, *Phys. Rev.* **182**, 1190 (1969).
- [49] P. Roussel-Chomaz, N. Alamanos, F. Auger, J. Barrette, B. Berthier, B. Fernandez, L. Papineau, H. Doubre, and W. Mittig, *Nucl. Phys. A* **477**, 345 (1988).
- [50] C. Olmer, M. Mermaz, M. Buenerd, C. K. Gelbke, D. L. Hendrie, J. Mahoney, D. K. Scott, M. H. Macfarlane, and S. C. Pieper, *Phys. Rev. C* **18**, 205 (1978).
- [51] C. A. Bertulani, *Phys. Rev. Lett.* **94**, 072701 (2005).